Singlet oxygen mediated iron-based Fenton-like catalysis under nanoconfinement

Zhichao Yang[a], Jieshu Qian[b], Anqing Yu[a], and Bingcai Pan[a,c,1]

[a]State Key Laboratory of Pollution Control and Resource Reuse, School of Environment, Nanjing University, 210023 Nanjing, China; [b]School of Environmental and Biological Engineering, Nanjing University of Science and Technology, 210094 Nanjing, China; and [c]Research Center for Environmental Nanotechnology (ReCENT), Nanjing University, 210023 Nanjing, China

Edited by Alexis T. Bell, University of California, Berkeley, CA, and approved February 20, 2019 (received for review November 12, 2018)

For several decades, the iron-based Fenton-like catalysis has been believed to be mediated by hydroxyl radicals or high-valent iron-oxo species, while only sporadic evidence supported the generation of singlet oxygen ($^1O_2$) in the Haber–Weiss cycle. Herein, we report an unprecedented singlet oxygen mediated Fenton-like process catalyzed by ∼2-nm Fe_2O_3 nanoparticles distributed inside multiwalled carbon nanotubes with inner diameter of ∼7 nm. Unlike the traditional Fenton-like processes, this delicately designed system was shown to selectively oxidize the organic dyes that could be adsorbed with oxidation rates linearly proportional to the adsorption affinity. It also exhibited remarkably higher degradation activity (22.5 times faster) toward a model pollutant methylene blue than its nonconfined analog. Strikingly, the unforeseen stability at pH value up to 9.0 greatly expands the use of Fenton-like catalysts in alkaline conditions. This work represents a fundamental breakthrough toward the design and understanding of the Fenton-like system under nanoconfinement, might cause implications in other fields, especially in biological systems.

Fenton-like catalysis | confinement | singlet oxygen | nanoparticles | water treatment

The seminal study by Fenton in 1894 (1) opened the door to create strong oxidants using Fe(II) and H_2O_2. This ubiquitous industrialized oxidation and its derivatives, i.e., Fenton-like reagents such as Fe(III)/H_2O_2, photo-/electro- Fenton, have been utilized in a versatile way in various fields including the cognition of biological stress response (2) and sensing (3), chemical analysis (4), molecular synthesis (5), material preparation (6), and environmental remediation (7) in the past century. Notwithstanding the obscure mechanism of Fenton's reaction (8–10), the main oxidative intermediate species involved in the bulk phase or at aqueous interfaces are proved to be the hydroxyl radicals (HO•) generated through the Haber–Weiss cycle (8, 9) or high-valent iron-oxo species [Fe(IV)=O/Fe(V)=O] produced via the Bray–Gorin mechanism (10, 11).

Recently, thriving researches on nanotechnology and nanomaterial have created tremendous opportunities for reinvestigation of various chemical reactions at the nanoscale, generating new insights on fundamental understanding and tools for various applications (12). For examples, under nanoconfinement provided by carbon nanotube (CNT), molecular-dynamics simulations showed pulse-like water transmission with concerted and rapid motion along the tube axis, as well as tunable channel occupancy and conductivity (13, 14). Similarly, a stable polymorphous crystal formed from ionic liquid [bmim][PF6] inside multiwalled carbon nanotubes (MWCNTs) exhibited a melting point of above 473 K, much higher than that of the unconfined analog (279 K) (15). With respect to RhMn nanoparticles inside CNTs, the electron-deficient interior surface of CNTs was shown to increase the tendency of confined Mn to accept electrons from CO, resulting in one order of magnitude improvement of C2 oxygenate yield from syngas (16).

Herein, we report an attempt to understand the behavior of the Fenton reaction under nanoconfinement of CNTs with size of ∼7 nm and demonstrate a singlet oxygen ($^1O_2$) mediated pathway. As shown in Fig. 1, two different structures were designed, i.e., distribution of Fe_2O_3 nanoparticles on the outer surface of CNT (upper route, referred to as Fe_2O_3/FCNT-L), anchoring of Fe_2O_3 nanoparticles inside the CNT for nanoconfinement (lower route, referred to as Fe_2O_3@FCNT-H). The former exhibited traditional Fenton-like reaction pathways with HO• as the main active species; however, an unprecedented reaction pathway with $^1O_2$ as the reactive intermediate was discovered in the latter design. We further used the latter as a catalyst for the oxidation of several organic dyes. Surprisingly, this nanoconfined system selectively oxidized the compounds that could be adsorbed with the reaction rates linearly proportional to the adsorption affinity. For the degradation of a model pollutant methylene blue (MB), the latter catalyst exhibited a remarkably faster kinetics (22.5 times) as well as an exceptionally higher pH stability (pH 5.0–9.0) than its nonconfined analog.

Results and Discussion

The inner diameters of the CNTs are estimated to be ∼7 nm (*SI Appendix*, Fig. S1). Representative high-angle dark-field scanning transmission electron microscopy (HADDF-STEM) images with energy-dispersive X-ray spectroscopy (EDX) elemental mapping (Fig. 2 *A* and *B* and *SI Appendix*, Fig. S2) clearly show that in Fe_2O_3/FCNT-L, nanoparticles are randomly distributed along the direction of CNT; however, in Fe_2O_3@FCNT-H, the distribution of the nanoparticles is dictated by the center of the CNT (pointed at by the red arrows). The insets of high-resolution transmission electron microscopy (HRTEM) images in both figures show the (311) crystalline lattice of Fe_2O_3 nanoparticles. The size-distribution histograms of Fe_2O_3 nanoparticles in both samples in Fig. 2*C* show the average size to be 2.4 nm (Fe_2O_3/FCNT-L) and

Significance

In the bulk phase, hydroxyl radical from the one-electron transfer and high-valent iron-oxo species from the O-atom transfer compete to be the reactive intermediates in the Fenton and related reactions. In the confined space at a nanoscale, however, the behavior of the Fenton reaction is elusive. Herein, we report an unprecedented singlet oxygen mediated Fenton's reaction occurred inside carbon nanotube with inner diameter of ∼7 nm, showing exotic catalytic activities, unforeseen adsorption-dependent selectivity, and pH stability for the oxidation of organic compounds. Our results suggest the use of Fenton's reaction in more scenarios than ever explored.

Author contributions: B.P. conceived the research; Z.Y., B.P., and J.Q. designed experiments; Z.Y. and A.Y. performed experiments; Z.Y., B.P., and J.Q. analyzed data; and Z.Y., B.P., and J.Q. wrote the paper.

The authors declare no conflict of interest.

This article is a PNAS Direct Submission.

[1]To whom correspondence should be addressed. Email: bcpan@nju.edu.cn.

This article contains supporting information online at www.pnas.org/lookup/suppl/doi:10.1073/pnas.1819382116/-/DCSupplemental.

Published online March 14, 2019.

ENGINEERING

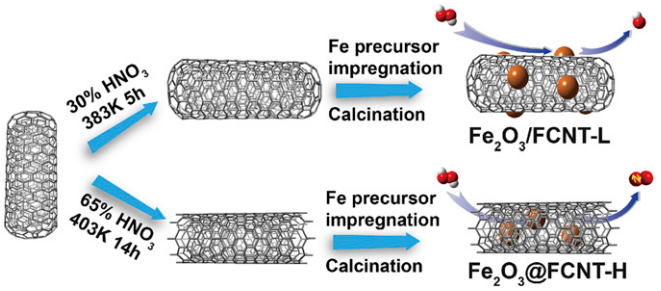

Fig. 1. Experimental design of this study.

1.9 nm (Fe_2O_3@FCNT-H). The mass fractions of Fe_2O_3 nanoparticles in both samples were determined to be similar, i.e., 2.09% for Fe_2O_3/FCNT-L and 1.93% for Fe_2O_3@FCNT-H. The XRD patterns in Fig. 2*D* show that both Fe_2O_3/FCNT-L and Fe_2O_3@FCNT-H exhibit four characteristic diffraction peaks of the (002), (100), (004), and (110) crystal planes of CNTs with typical hexagonal graphite structure. Meanwhile, two weak peaks at 35.9° and 62.3° appear in both samples (Fig. 2*D*), highly suspected to be the diffraction of (311) and (440) crystal planes of Fe_2O_3 (Joint Committee on Powder Diffraction Standards 04–0755), which was further confirmed by the sole presence of Fe^{3+} species by ^{57}Fe Mössbauer spectra of both samples (*SI Appendix*, Fig. S3) (17, 18).

The Raman spectra (*SI Appendix*, Fig. S4) show that in comparison with CNT, the two samples exhibit an adsorption band at around 280 cm^{-1} after the Fe_2O_3 loading, which could be assigned to the E_g Fe-O vibration mode (19). The blue shift of this band from 281.2 cm^{-1} of Fe_2O_3/FCNT-L to 285.2 cm^{-1} of Fe_2O_3@FCNT-H indicates the interaction of Fe_2O_3 with the inner surface of the CNT in Fe_2O_3@FCNT-H (19). The Fe 2p XPS spectra in Fig. 2*E* show surprising difference of the Fe 2p peak intensities between both samples, i.e., much weaker Fe 2p peaks of Fe_2O_3@FCNT-H than Fe_2O_3/FCNT-L despite their similar Fe contents. This is probably due to the limited probe depth of the photoelectrons (3–5 nm) for the detection of Fe_2O_3 inside the CNT. The N_2 adsorption–desorption isotherms are shown in Fig. 2*F*, from which the Brunner–Emmet–Teller (BET)-specific surface areas are calculated to be 197 $m^2 \cdot g^{-1}$ (Fe_2O_3/FCNT-L) and 206 $m^2 \cdot g^{-1}$ (Fe_2O_3@FCNT-H), and the BJH pore volumes are 0.59 and 0.43 $cm^3 \cdot g^{-1}$, respectively.

We first identified the generated active species in various systems. The electron spin resonance (ESR) spectra (Fig. 3*A*) show that, by using 5,5-dimethyl-1-pyrroline *N*-oxide (DMPO) as the trapping agent, one could observe the quadruple peak signals of DMPO-HO• (1:2:2:1, $\alpha_N = \alpha_H = 14.9$ G, g = 2.0055) in Fe_2O_3/FCNT-L/H_2O_2 and Fe_2O_3/H_2O_2 systems, which are expected in traditional Fenton-like systems. On the contrary, the DMPO-HO• signal was not detected in Fe_2O_3@FCNT-H/H_2O_2 system at all. Instead, when 2,2,6,6-tetramethyl-4-piperidinol (TEMP) was used as the trapping agent, a triplet peak signal (1:1:1, $\alpha_N = 16.9$ G, g = 2.0054) of 2,2,6,6-tetramethyl-4- piperidinol-*N*-oxyl radical (TMPN) emerged, indicating the presence of $^1O_2$ (20, 21). Not surprisingly, it was not detected in both Fe_2O_3/FCNT-L/H_2O_2 and Fe_2O_3/H_2O_2 systems. More credible evidence was discovered based on the determination of indicative products from the specific reactions between classical chemical probe 9,10-diphenylanthracene (DPA) and $^1O_2$ (22). As presented in Fig. 3*B*, the chromatographic peak of anthracene endoperoxide ($DPAO_2$) appeared in Fe_2O_3@FCNT-H/H_2O_2 system and its concentration also increased when the dosage of Fe_2O_3@FCNT-H increased from 1.5×10^{-2} $g L^{-1}$ to 2.5×10^{-2} $g L^{-1}$, clearly showing the generation of $^1O_2$.

We further evaluated the role of $^1O_2$ in Fe_2O_3@FCNT-H/H_2O_2 system by calculating the material balance of furfuryl alcohol (FFA) oxidation (see *SI Appendix*, *Texts S1* and *S2* for details). Consistent with the results from previous studies (23, 24), three typical products, $C_5H_6O_4$ (*m/z* 129.0181 in negative ionization mode), $C_4H_4O_3$ (*m/z* 99.0072 in negative ionization

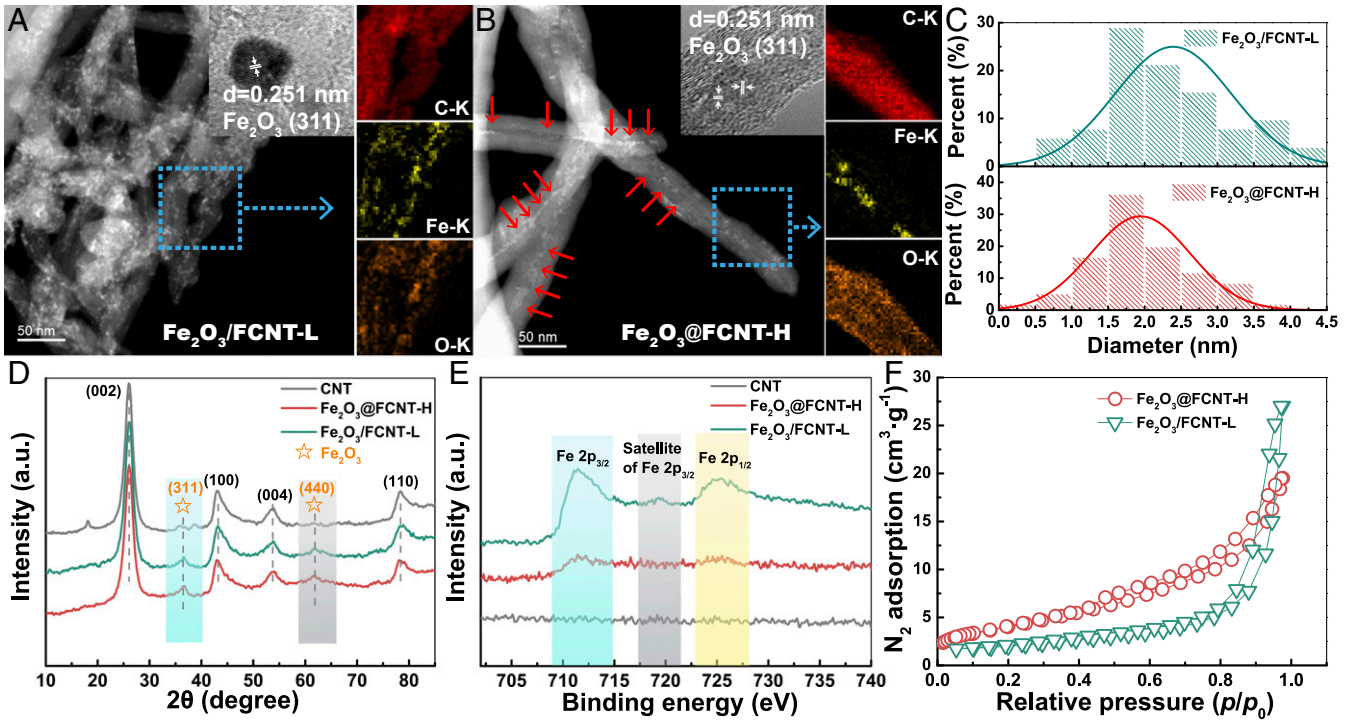

Fig. 2. Structure of the catalysts. (*A* and *B*) Representative HADDF-STEM images of Fe_2O_3/FCNT-L and Fe_2O_3@FCNT-H (*Insets*) HRTEM images of the Fe_2O_3 nanoparticles; dexter figures show the EDX elemental mappings of the selected area. (*C*) Size-distribution histograms of the Fe_2O_3 nanoparticles in both samples. (*D*) XRD patterns and (*E*) Fe 2p XPS spectra of CNT, Fe_2O_3/FCNT-L and Fe_2O_3@FCNT-H. (*F*) N_2 adsorption–desorption isotherms of Fe_2O_3/FCNT-L and Fe_2O_3@FCNT-H.

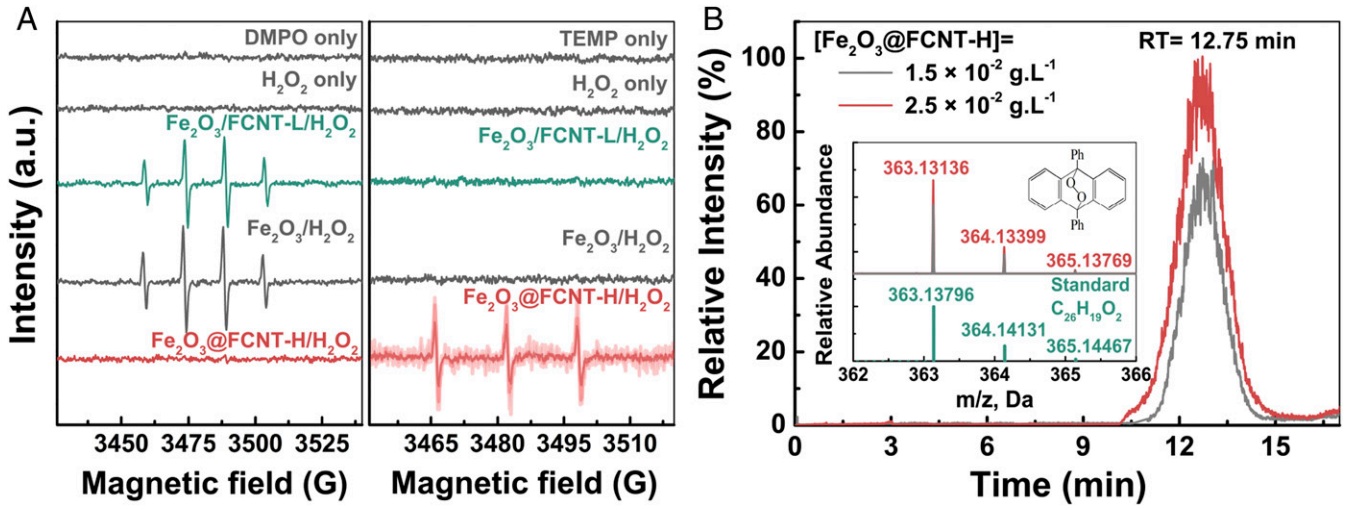

Fig. 3. Reactive intermediates identification. (*A*) ESR spectra of different systems using DMPO and TEMP as trapping agents. (*B*) UHPLC/MS chromatogram of the typical $DPAO_2$ from the oxidation of DPA in Fe_2O_3@FCNT-H/H_2O_2 system. Reaction conditions: pH = 5.0, T = 293.2 K, [Fe_2O_3@FCNT-H] = 1.5 × 10^{-2} g·L^{-1}, [H_2O_2] = 50 mM, [DMPO] = [TEMP] = 50 mM for *A*, and [DPA] = 10 μM, [ACN] = 50 mM, reaction time = 60 min for *B*.

mode), and $C_5H_6O_3$ (*m*/*z* 113.0228 in negative ionization mode) were detected at the retention time of 5.38, 5.86, and 7.56 min, respectively (see Fig. 4*A* and *SI Appendix*, Fig. S5 for details). Moreover, a >98% conversion to three classical products from the oxidation of FFA indicated the exclusive role of $^1O_2$ as the reactive intermediate in Fe_2O_3@FCNT-H/H_2O_2 system (Fig. 4*B*). It is accepted that $^1O_2$ could be generated via oxidation, disproportionation, and/or decomposition of peroxy-metal species in the H_2O_2-based systems catalyzed by halide ions, metal salts, and minerals (e.g., hypochlorite, molybdate, and lanthanum oxide) (25, 26). Nevertheless, the generation of $^1O_2$ in the iron-based Fenton-like reaction was challenged in the bulk phase from both kinetic and thermodynamic points of view (25, 26). Our solid proof of the exclusive role of $^1O_2$ in Fe_2O_3@FCNT-H/H_2O_2 system might suggest that the nanoconfinement changes the Fenton-like reaction pathway both kinetically and thermodynamically.

We are intrigued to investigate the catalytic performance of the nanoconfined Fenton's catalyst. As presented in Fig. 5*A*, using MB as a model pollutant, one can see that in the absence of H_2O_2, both samples exhibited noticeable MB removal, presumably due to the adsorption of MB. However, in the presence of H_2O_2, Fe_2O_3@FCNT-H exhibited a remarkably higher MB degradation rate with the value of pseudo–first-order constant (k_{app}) = 5.25 × 10^{-2} min^{-1}, which is 22.5 times higher than that of Fe_2O_3/FCNT-L (2.33 × 10^{-3} min^{-1}) (*SI Appendix*, Fig. S6). Meanwhile, Fe_2O_3@FCNT-H/H_2O_2 is more effective than Fe_2O_3/FCNT-L/H_2O_2 in reducing the total organic carbon (25 vs. 15%) in 60 min (*SI Appendix*, Fig. S7). As shown in Fig. 5*B*, H_2O_2 alone has negligible effect on the MB removal even with the presence of Fe_2O_3; CNT/H_2O_2 has identical effect as CNT alone due to the adsorption effect (27). Samples of Fe_2O_3 nanoparticles loaded on various commercial substrates including carboxylated CNTs (CNT-COOH), SBA-15, and graphene oxide (GO) also exhibit significantly lower MB removal activities than Fe_2O_3@FCNT-H (*SI Appendix*, Fig. S8). All these results emphasize the key role of the interaction of the Fe_2O_3 nanoparticles inside the CNT for the surprisingly high MB removal activity of Fe_2O_3@FCNT-H.

The versatility of Fe_2O_3@FCNT-H under different conditions is of great general importance. The MB removal by the Fe_2O_3@FCNT-H/H_2O_2 system under different conditions is shown in *SI Appendix*, Fig. S9 with the accompanying discussion. The key information one could acquire is that the generation of $^1O_2$, represented by the apparent MB degradation kinetics, can be effectively elevated by increasing catalyst dosage, H_2O_2 concentration, and reaction temperature.

We then investigated the reusability and pH stability of Fe_2O_3@FCNT-H. Fig. 5*C* shows a slight deactivation of Fe_2O_3@FCNT-H for five consecutive MB additions, presumably due to either the gradual occupation of active sites or the competitive reaction with $^1O_2$ by the cumulative degradation products (28). However, the catalytic activity was fully recovered after washing with ethanol for later use without detectable ion leaching, suggesting excellent reusability of Fe_2O_3@FCNT-H. One can see from Fig. 5*D* that the value of k_{app} increases with the increase of pH

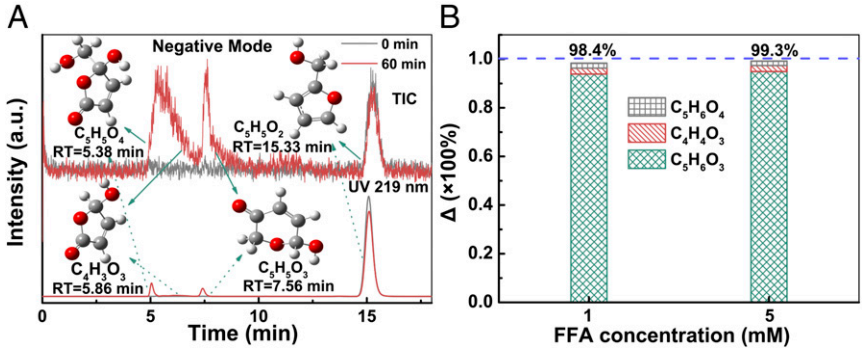

Fig. 4. The mass balance of FFA oxidation. (*A*) UHPLC/MS chromatogram of the typical products from the oxidation of FFA in Fe_2O_3@FCNT-H/H_2O_2 system. Mass spectra of the products are available in *SI Appendix*, Fig. S5. (*B*) The mass balance for the oxidation of FFA in Fe_2O_3@FCNT-H/H_2O_2 system. Reaction conditions: pH = 5.0, T = 293.2 K, [Fe_2O_3@FCNT-H] = 1.5 × 10^{-2} g·L^{-1}, [H_2O_2] = 50 mM, [FFA] = 1/5 mM, [MeOH] = 50 mM, reaction time = 60 min.

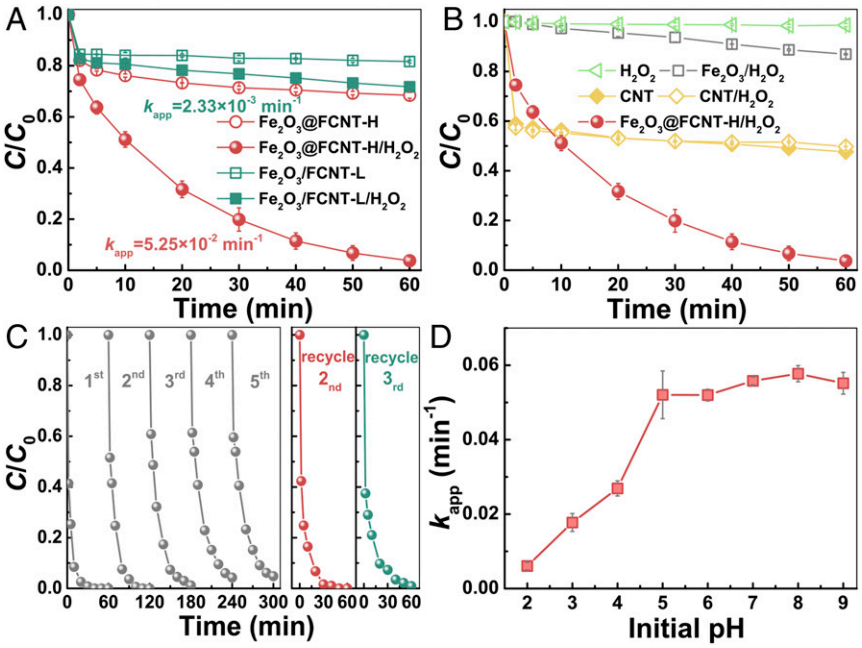

Fig. 5. Catalytic properties of Fe_2O_3@FCNT-H and Fe_2O_3/FCNT-L. (*A*) Plots of MB concentrations versus time of Fe_2O_3@FCNT-H and Fe_2O_3/FCNT-L with/without H_2O_2. (*B*) Plots of MB concentrations versus time of different systems. (*C*) Five consecutive MB removal experiments with two more regeneration studies of Fe_2O_3@FCNT-H. (*D*) The plot of k_{app} versus solution pH. Reaction conditions: T = 293.2 K, [MB] = 10 μM, [H_2O_2] = 50 mM, pH = 5.0 for *A*–*C* and 3.0–9.0 for *D*, [catalysts] (except Fe_2O_3) = 1.5×10^{-2} g·L^{-1} for *A*, *B*, and *D* and 4.0×10^{-2} g·L^{-1} for *C*, [Fe_2O_3] = 1.0×10^{-1} g·L^{-1} in *B*.

value from 2.0 to 5.0, and unprecedentedly, remains stable as the pH value further increases to 9.0 (*SI Appendix*, Fig. S10). On the contrary, k_{app} of Fe_2O_3/FCNT-L/H_2O_2 system decreased as the pH value increased from 3.0 to 9.0 (*SI Appendix*, Fig. S11), which is a common phenomenon observed in traditional Fenton-like systems (29, 30). We discuss the effect of pH on MB removal of our Fe_2O_3@FCNT-H/H_2O_2 system in detail (*SI Appendix*, *Part S1*). Based on the results of *SI Appendix*, Figs. S12–S15, we reckon that pH plays a crucial role in the MB removal through affecting the $^1O_2$ generation as well as the MB adsorption. The precise understanding for this unusual phenomenon still needs more elaborate future exploration; nevertheless, it presents a much more improved suitability in a broad pH range than the classical Fenton-like systems.

Considering $^1O_2$ is not such a general oxidant as HO•, we list a number of both organic and inorganic species that have been studied previously in $^1O_2$-mediated oxidation systems (*SI Appendix*, Table S1). In this work, the catalytic degradation of several different compounds [i.e., cationic ones including methyl violet, crystal violet, chrysoidine, and malachite green oxalate; anionic ones including methyl orange (MO) and chromotrope 2R (C2R) and neutral aniline] in Fe_2O_3@FCNT-H/H_2O_2 system was carried out to further demonstrate the versatility of Fe_2O_3@FCNT-H (*SI Appendix*, Fig. S16). We show that anionic compounds including MO and C2R and neutral aniline could not be effectively adsorbed by Fe_2O_3@FCNT-H; consequently, only a small fraction was degraded. Those cationic compounds which could be efficiently adsorbed were rapidly degraded. Fig. 6*A* shows the values of k_{app} versus $q_{e,cal}$ of Fe_2O_3@FCNT-H toward various cationic compounds. One can see that the value of k_{app} is linearly proportional to the value of $q_{e,cal}$ calculated from the pseudo–second-order adsorption kinetics ($r > 0.97$) (*SI Appendix*, Fig. S17). This result clearly shows an exotic adsorption-dependent removal feature of Fe_2O_3@FCNT-H, while the degradation kinetics is normally proportionally to the concentration of HO• and irrelevant to adsorption in traditional Fenton's reactions (31). As a consequence, our nanoconfined Fenton's reagent could be used to selectively degrade the compounds which are prone to be adsorbed (*SI Appendix*, Fig. S18). One might also be interested in the precise location where the pollutant is oxidized by the $^1O_2$, i.e., on the outer surface of CNT or inside the CNT. Although we have our preferential guess of the latter based on the adsorption-dependent process (32–39), we do not have solid proof at this point. We would like to leave this question for further exploration.

Based on the previous results and discussion, a possible catalytic pathway of Fe_2O_3@FCNT-H/H_2O_2 system for pollutant

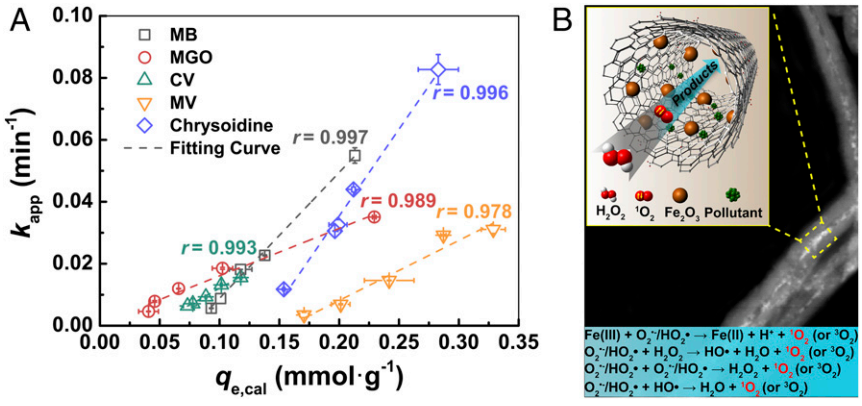

Fig. 6. The role of adsorption and possible mechanism scheme. (*A*) Plots of k_{app} versus $q_{e,cal}$ manipulated through the addition of Al^{3+} for Fe_2O_3@FCNT-H toward various cationic compounds. Reaction conditions: pH = 5.0, T = 293.2 K, [Fe_2O_3@FCNT-H] = 1.5×10^{-2} g·L^{-1}, [target compounds] = 10 μM, [H_2O_2] = 50 mM, [Al^{3+}] = 0.1–1 mM. (*B*) Illustration of possible mechanism of pollutants degradation in Fe_2O_3@FCNT-H/H_2O_2 system.

degradation is illustrated as a scheme in Fig. 6*B*. Since both light and oxygen do not contribute to the process (*SI Appendix*, Fig. S19), we assert that H_2O_2 is the only source for $^1O_2$ generation in Fe_2O_3@FCNT-H/H_2O_2 system, via the gain of two electrons by H_2O_2 to generate $^1O_2$. There are three possible oxidation pathways of H_2O_2, a one-step two-electron transfer and two-step one-electron transfer with or without the contribution of high-valent iron-oxo species. The one-step two-electron transfer involving the reduction of Fe(III) to Fe(I) only exists in Fe-catalyzed cross-coupling reactions theoretically (40). The two-step one-electron transfer involving the oxidation of H_2O_2 by high-valent iron-oxo species depicted by Collins and coworkers could also be excluded because the pivotal intermediate could not be detected (see DMSO quenching experiment for the detection of high-valent iron-oxo species in *SI Appendix*, Fig. S13) (41). In contrast, the two-step one-electron transfer following the Haber–Weiss cycle is the most likely pathway for $^1O_2$ generation. In the first step, the Fe(III) species on the surface of the Fe_2O_3 nanoparticles inside CNT is reduced by H_2O_2 to produce HO_2•/$O_2^{\cdot-}$, which can be further supported by the obvious shift to the lower region by 0.7 eV with the addition of H_2O_2 in in situ X-ray absorption near edge structure (XANES) analysis as depicted in *SI Appendix*, Fig. S20. The nanoconfinement by CNT poses strong electronic interaction with Fe_2O_3 nanoparticles due to the electron-deficient concave surface, facilitating this process compared with the Fe_2O_3 nanoparticles outside (42–44). The second step deals with several possibilities contributing to the oxidation of HO_2•/$O_2^{\cdot-}$ to form $^1O_2$, since we have demonstrated HO_2•/$O_2^{\cdot-}$ to be the key intermediate for $^1O_2$ generation (*SI Appendix*, *Part S1* and Figs. S12–S14). (*i*) One is the oxidation by Fe(III) in the favored spin state, regulated by the confined space and the unique electronic structure of CNTs (25). (*ii*) The second is the radical–radical reactions including HO_2•/$O_2^{\cdot-}$ recombination and the reaction between HO_2•/$O_2^{\cdot-}$ and HO• (45–48). The Gibbs free energy for HO_2•/$O_2^{\cdot-}$ recombination is −6.4 kcal·mol^{-1} at pH 7, indicating its thermodynamic spontaneity (45). However, we could not obtain even tiny evidence for the presence of HO• in Fe_2O_3@FCNT-H/H_2O_2 system by chemical quenching or trapping experiment (Fig. 3*A* and *SI Appendix*, Fig. S13), which is probably due to either the slow diffusion of quenching molecules or the accelerated radical recombination (49). Consequently, we do not exclude the possible contribution of HO• in the $^1O_2$ generation but we reckon its contribution is small. (*iii*) The third is the reaction between HO_2•/$O_2^{\cdot-}$ and H_2O_2 (50). The reaction constant is ∼3–10 magnitude smaller than those in (*i*) and (*ii*) (*SI Appendix*, Table S2); however, its contribution to the $^1O_2$ generation might be compensated by significantly higher H_2O_2 concentration than radicals. These three possible reactions could be well accelerated via the enrichment as well as the limited migration of the as-formed radicals in the confined space (37, 48, 49). Another key role of the nanoconfinement in Fe_2O_3@FCNT-H/H_2O_2 system is suspected to largely improve the selectivity of these reactions to produce $^1O_2$, rather than O_2 in the traditional bulk systems (51).

In conclusion, by loading ∼2 nm Fe_2O_3 nanoparticles inside the confined space of CNT with inner diameter of ∼7 nm, we are able to create a Fenton-like catalyst Fe_2O_3@FCNT-H showing completely different catalytic pathway from traditional Fenton-like catalyst Fe_2O_3/FCNT-L, in which Fe_2O_3 nanoparticles are loaded on the outer surface of CNT. The $^1O_2$ radical was observed as the main reactive intermediate generated in Fe_2O_3@FCNT-H/H_2O_2 system, other than HO• that was generated in Fe_2O_3/FCNT-L/H_2O_2 system and has been accepted as the main active species in the Fenton-like systems for many years. Meanwhile, a 22.5× faster MB degradation kinetics in Fe_2O_3@FCNT-H/H_2O_2 than Fe_2O_3/FCNT-L/H_2O_2 was obtained. Moreover, Fe_2O_3@FCNT-H exhibited surprisingly high stability over a broad pH range from 5.0 to 9.0, while it is almost impossible to utilize traditional Fenton-like catalyst under alkaline conditions. We also demonstrated that the oxidation rates of different pollutants in the Fe_2O_3@FCNT-H/H_2O_2 system are highly dependent on the adsorption affinity between the pollutants and the catalyst. Our work has presented a delicate design of Fenton's catalyst using nanoconfinement for pollutant removal with exceptional activity and pH suitability, and also, has laid a milestone toward the mechanistic understanding of the Fenton-like reactions under nanoconfinement. We hope our work could stimulate the researchers to use nanoconfined Fenton's reaction in various applications especially biological systems to realize selective and efficient oxidation.

Methods

The chemicals and materials used in the experiments are described in *SI Appendix*, *Text S3*.

Preparation of Catalysts. The catalysts used in this work were synthesized according to a slightly modified method (42, 43). Pristine MWCNTs (pCNT) were first refluxed in concentrated HNO_3 solution (65 wt %) at 403 ± 5 K under magnetic stirring for 14 h. After being filtered and washed with ultrapure water until the pH value of the filtrate reached ∼6.1, the solids were ultrasonically dispersed in the ultrapure water and lyophilized (Freezone 2.5; Labconco) for better dispersion of the particles (denoted as FCNT-H). Sample FCNT-L was prepared by refluxing pCNT in HNO_3 solution (30 wt %) at 383 ± 5 K for 5 h. Sample of CNT-COOH was prepared by refluxing commercial sample in HCl solution (38 wt %) at 343 K for 12 h to remove residual metal impurities. $Fe(NO_3)_3.9H_2O$ (0.361 g) was dissolved in 250 mL acetone to serve as an iron precursor. Afterward, each of 0.20 g supporter (i.e., FCNT-H, FCNT-L, CNT-COOH, SBA-15, and GO) was dispersed in 20 mL Fe(III)/acetone solution, respectively. The mixed solution was first stirred for 1 h and then treated by ultrasonication for 4 h, while temperature was kept constant at 293.2 ± 0.3 K using a thermostat (THD-5015; Tianheng). As the slow evaporation of acetone, Fe(III) was deposited on the inner or outer surface of the host materials. The as-obtained solid was gradually heated to 413 K in air and kept for 10 h. After being washed with ultrapure water, we obtained samples of Fe_2O_3@FCNT-H, Fe_2O_3/FCNT-L, Fe_2O_3/CNT-COOH, Fe_2O_3/SBA-15, and Fe_2O_3/GO, respectively. The Fe loading of the catalysts was 2 wt % unless else stated. The unsupported iron oxides and FCNT-H for comparison were prepared using a similar method without adding FCNT-H or iron precursor, respectively. Catalysts were stored as the form of aqueous suspensions via direct ultrasonication for 20 min. To maintain homogeneity, the stock suspension was periodically treated by ultrasonication for 10 min before use.

Characterization of Catalysts. The loaded Fe content was determined by an atomic absorption spectrophotometer (AA-7000; Shimadzu) after acidic digestion overnight using the concentrated HCl solution assisted by ultrasonic treatment in a sealed polytetrafluoroethylene (PTFE) bottle. The crystalline structures of the catalysts were determined by XRD (D-MAX Rapid-II; Rigaku) using Mo Kα radiation (λ = 0.7093 Å). For better analysis and comparison with the data from XRD in Cu Kα radiation, the obtained XRD spectra were transferred according to the Bragg equation (*SI Appendix*, *Text S4*). The analysis of surface properties was conducted using N_2 adsorption–desorption test at 77 K (NOVA3000; Quantachrome). XPS (K-Alpha; Thermo) was used to determine the element chemical states near the surface region. The ^{57}Fe Mössbauer spectra were recorded by proportional counter on Topologic 500 spectrometer (MFD-500AV) with ^{57}Co (Rh) as a λ-ray source at room temperature. The morphologies were examined by TEM (TECNAI G^2 F20; FEI) at an accelerating voltage of 200 kV. STEM was performed to characterize the dispersion and configuration of the catalysts. Individual heavy atoms can be discerned in the HAADF images. Moreover, STEM-EDX was conducted to map the abundance of C, O, and Fe in the catalysts. Raman spectra were recorded with a LabRAM Aramis Raman spectrometer (Horiba Scientific) with an Ar^+ laser at 532 nm. In situ XANES analysis was carried out at room temperature in Beijing Synchrotron Radiation Facility with Fe foil and Fe_2O_3 as reference, *K*-edge energies of which were located at 7,112.1 and 7,126.6 eV, respectively.

Examination of Catalysts. The degradation experiments were conducted in a 50-mL conical flask under magnetic stirring at 293.2 ± 0.3 K. Reactions were initiated by simultaneous addition of the catalyst suspension and H_2O_2 into the solution containing target dyes. Adsorption experiments were also conducted in a 50-mL conical flask on a rotary shaker at 150 rpm at 293.2 ± 0.3 K. The experiment was initiated after adding the catalyst suspension to

the solutions of various target compounds with/without Al^{3+} ions (0.1–1 mM) at pH 5.0 unless specified. The pH values of solutions were adjusted by diluted HNO_3 and NaOH. Reaction aliquots were periodically taken and filtered through a membrane (0.22 μm) to remove the solid catalysts for analysis. The detailed experimental conditions are presented in the legend of each figure. To test the stability and reusability of Fe_2O_3@FCNT-H, a 1.75 L reactor was used to avoid the loss of catalyst during recycle (see *SI Appendix, Text S5* for details). The used catalysts were collected by suction filtration and simply washed with ethanol and ultrapure water.

The concentrations of organic dyes were analyzed at the maximum absorption wavelength by a UV-vis spectrophotometer (T6; Beijing Persee) (*SI Appendix*, Table S3). An ultrahigh-performance liquid chromatography (UHPLC, Ultimate 3000; Thermo) with a symmetry C18 column was used to analyze FFA, aniline, and 4-CP (*SI Appendix*, Table S4). TOC was measured by subtracting the concentration of inorganic carbon from the total carbon on a Shimadzu TOC-V_{CPH} analyzer (Japan) and the quantification was based on a standard calibration in the range of 0–3 $mg{\cdot}L^{-1}$. The concentration of leached iron species was determined through 1,10-phenanthroline method after reduction by hydroxylamine hydrochloride with the limit of detection of 0.36 μM. ESR spectra of DMPO-$HO^{\bullet}$, DMPO-OOH, and TMPN were obtained with an ESR A300 spectrometer (Bruker). The detailed operation methods are presented in *SI Appendix, Text S6*. A Thermo U3000 ultrahigh performance liquid chromatography coupled with a Thermo Q-Exactive Focus MS with an electron spray ionization source was employed to identify the intermediate products from DPA oxidation and FFA oxidation (see *SI Appendix, Text S1* for details). The concentration of products from FFA oxidation was calculated as described in *SI Appendix, Text S2*.

ACKNOWLEDGMENTS. The authors are grateful to Beijing Synchrotron Radiation Facility for XANES analysis and the High Performance Computing Center of Nanjing University for doing the numerical calculations in this paper on its blade cluster system. We thank Prof. Xiulian Pan, Dalian Institute of Chemical Physics, for the advice on catalyst preparation and Prof. Peng Wang, College of Engineering and Applied Sciences, Nanjing University, for the help in TEM and STEM-EDX characterization. Dr. Chao Shan provided insightful discussion during the revision. This study was financially supported by Natural Science Foundation of China (Grant 21177059/51761165011), National Key R&D Program of China (Grant 2016YFA0203104), and Natural Science Foundation of Jiangsu Province (Grant BK20160653).

1. Fenton HJH (1894) Oxidation of tartaric acid in presence of iron. *J Chem Soc Trans* 65: 899–910.
2. Liu Q, et al. (2004) A Fenton reaction at the endoplasmic reticulum is involved in the redox control of hypoxia-inducible gene expression. *Proc Natl Acad Sci USA* 101: 4302–4307.
3. Lee JW, Helmann JD (2006) The PerR transcription factor senses H_2O_2 by metal-catalysed histidine oxidation. *Nature* 440:363–367.
4. Shelor CP, et al. (2011) Fenton digestion of milk for iodinalysis. *Anal Chem* 83: 8300–8307.
5. Chen MS, White MC (2007) A predictably selective aliphatic C-H oxidation reaction for complex molecule synthesis. *Science* 318:783–787.
6. Feng G, et al. (2016) Accelerated crystallization of zeolites via hydroxyl free radicals. *Science* 351:1188–1191.
7. Brillas E, Sirés I, Oturan MA (2009) Electro-Fenton process and related electrochemical technologies based on Fenton's reaction chemistry. *Chem Rev* 109:6570–6631.
8. Walling C (1975) Fenton's reagent revisited. *Acc Chem Res* 8:125–131.
9. Pignatello JJ, Oliveros E, MacKay A (2006) Advanced oxidation processes for organic contaminant destruction based on the Fenton reaction and related chemistry. *Crit Rev Environ Sci Technol* 36:1–84.
10. Enami S, Sakamoto Y, Colussi AJ (2014) Fenton chemistry at aqueous interfaces. *Proc Natl Acad Sci USA* 111:623–628.
11. Bossmann SH, et al. (1998) New evidence against hydroxyl radicals as reactive intermediates in the thermal and photochemically enhanced Fenton reactions. *J Phys Chem A* 102:5542–5550.
12. Miners SA, Rance GA, Khlobystov AN (2016) Chemical reactions confined within carbon nanotubes. *Chem Soc Rev* 45:4727–4746.
13. Hummer G, Rasaiah JC, Noworyta JP (2001) Water conduction through the hydrophobic channel of a carbon nanotube. *Nature* 414:188–190.
14. Liu X, Pan X, Zhang S, Han X, Bao X (2014) Diffusion of water inside carbon nanotubes studied by pulsed field gradient NMR spectroscopy. *Langmuir* 30:8036–8045.
15. Chen S, Wu G, Sha M, Huang S (2007) Transition of ionic liquid [bmim][PF6] from liquid to high-melting-point crystal when confined in multiwalled carbon nanotubes. *J Am Chem Soc* 129:2416–2417.
16. Pan X, et al. (2007) Enhanced ethanol production inside carbon-nanotube reactors containing catalytic particles. *Nat Mater* 6:507–511.
17. Zboril R, Mashlan M, Petridis D (2002) Iron(III) oxides from thermal processes-synthesis, structural and magnetic properties, Mössbauer spectroscopy characterization, and applications. *Chem Mater* 14:969–982.
18. Fierro G, Moretti G, Ferraris G, Andreozzi GB (2011) A Mössbauer and structural investigation of Fe-ZSM-5 catalysts: Influence of Fe oxide nanoparticles size on the catalytic behaviour for the NO-SCR by C_3H_8. *Appl Catal B* 102:215–223.
19. Chen W, Pan X, Bao X (2007) Tuning of redox properties of iron and iron oxides via encapsulation within carbon nanotubes. *J Am Chem Soc* 129:7421–7426.
20. Moan J, Wold E (1979) Detection of singlet oxygen production by ESR. *Nature* 279: 450–451.
21. Song B, Wang G, Tan M, Yuan J (2006) A europium(III) complex as an efficient singlet oxygen luminescence probe. *J Am Chem Soc* 128:13442–13450.
22. Miyamoto S, Martinez GR, Martins APB, Medeiros MHG, Di Mascio P (2003) Direct evidence of singlet molecular oxygen [O_2 ($^1\Delta_g$)] production in the reaction of linoleic acid hydroperoxide with peroxynitrite. *J Am Chem Soc* 125:4510–4517.
23. Braun AM, et al. (1999) (2+4)-Cycloaddition with singlet oxygen. 17O-investigation of the reactivity of furfuryl alcohol endoperoxide. *Photochem Photobiol* 70:868–874.
24. Halladja S, Ter Halle A, Aguer JP, Boulkamh A, Richard C (2007) Inhibition of humic substances mediated photooxygenation of furfuryl alcohol by 2,4,6-trimethylphenol. Evidence for reactivity of the phenol with humic triplet excited states. *Environ Sci Technol* 41:6066–6073.
25. Evans DF, Upton MW (1985) Studies on singlet oxygen in aqueous solution. Part 4. The 'spontaneous' and catalysed decomposition of hydrogen peroxide. *J Chem Soc Dalton Trans* 12:2525–2529.
26. Aubry JM (1986) Search for singlet oxygen in the decomposition of hydrogen peroxide by mineral compounds in aqueous solutions. *J Am Chem Soc* 17:5844–5849.
27. Pignatello JJ, Mitch WA, Xu W (2017) Activity and reactivity of pyrogenic carbonaceous matter toward organic compounds. *Environ Sci Technol* 51:8893–8908.
28. Snyder BER, et al. (2018) Mechanism of selective benzene hydroxylation catalyzed by iron-containing zeolites. *Proc Natl Acad Sci USA* 115:12124–12129.
29. Yang X, Xu X, Xu J, Han Y (2013) Iron oxychloride (FeOCl): An efficient fenton-like catalyst for producing hydroxyl radicals in degradation of organic contaminants. *J Am Chem Soc* 135:16058–16061.
30. Pouran SR, Raman AAA, Wan MAWD (2014) Review on the application of modified iron oxides as heterogeneous catalysts in Fenton reactions. *J Clean Prod* 64:24–35.
31. Navalon S, Dhakshinamoorthy A, Alvaro M, Garcia H (2011) Heterogeneous fenton catalysts based on activated carbon and related materials. *ChemSusChem* 4: 1712–1730.
32. Dujardin E, Ebbesen TW, Hiura H, Tanigaki K (1994) Capillarity and wetting of carbon nanotubes. *Science* 265:1850–1852.
33. Yang H, Zhang L, Zhong L, Yang Q, Li C (2007) Enhanced cooperative activation effect in the hydrolytic kinetic resolution of epoxides on [Co(salen)] catalysts confined in nanocages. *Angew Chem Int Ed Engl* 46:6861–6865.
34. Lan Y, Yang L, Zhang M, Zhang W, Wang S (2010) Microreactor of Pd nanoparticles immobilized hollow microspheres for catalytic hydrodechlorination of chlorophenols in water. *ACS Appl Mater Interfaces* 2:127–133.
35. Chen Z, Guan Z, Li M, Yang Q, Li C (2011) Enhancement of the performance of a platinum nanocatalyst confined within carbon nanotubes for asymmetric hydrogenation. *Angew Chem Int Ed Engl* 50:4913–4917.
36. Pan X, Bao X (2011) The effects of confinement inside carbon nanotubes on catalysis. *Acc Chem Res* 44:553–562.
37. Li B, et al. (2012) Hydration of epoxides on [Co^{III}(salen)] encapsulated in silica-based nanoreactors. *Angew Chem Int Ed* 124:11685–11689.
38. Liu C, et al. (2014) Yolk-shell Fe^0@SiO_2 nanoparticles as nanoreactors for fenton-like catalytic reaction. *ACS Appl Mater Interfaces* 6:13167–13173.
39. Zeng T, Zhang X, Wang S, Niu H, Cai Y (2015) Spatial confinement of a Co_3O_4 catalyst in hollow metal-organic frameworks as a nanoreactor for improved degradation of organic pollutants. *Environ Sci Technol* 49:2350–2357.
40. Hu L, Chen H (2017) Substrate-dependent two-state reactivity in iron-catalyzed alkene [2+2] cycloaddition reactions. *J Am Chem Soc* 139:15564–15567.
41. Ghosh A, et al. (2008) Catalase-peroxidase activity of iron(III)-TAML activators of hydrogen peroxide. *J Am Chem Soc* 130:15116–15126.
42. Chen W, Pan X, Willinger MG, Su DS, Bao X (2006) Facile autoreduction of iron oxide/carbon nanotube encapsulates. *J Am Chem Soc* 128:3136–3137.
43. Chen W, Fan Z, Pan X, Bao X (2008) Effect of confinement in carbon nanotubes on the activity of Fischer-Tropsch iron catalyst. *J Am Chem Soc* 130:9414–9419.
44. Chen W, et al. (2011) Enhanced visible-light activity of titania via confinement inside carbon nanotubes. *J Am Chem Soc* 133:14896–14899.
45. Koppenol WH (1976) Reactions involving singlet oxygen and the superoxide anion. *Nature* 262:420–421.
46. Khan AU, Kasha M (1994) Singlet molecular oxygen in the Haber-Weiss reaction. *Proc Natl Acad Sci USA* 91:12365–12367.
47. Ivanova IP, et al. (2012) Mechanism of chemiluminescence in Fenton reaction. *J Biophys Chem* 3:88–100.
48. Dou X, et al. (2013) Production of superoxide anion radicals as evidence for carbon nanodots acting as electron donors by the chemiluminescence method. *Chem Commun* 49:5871–5873.
49. Foley S, et al. (2004) Radiolysis of confined water: Production and reactivity of hydroxyl radicals. *Angew Chem Int Ed Engl* 44:110–112.
50. MacManus-Spencer LA, McNeill K (2005) Quantification of singlet oxygen production in the reaction of superoxide with hydrogen peroxide using a selective chemiluminescent probe. *J Am Chem Soc* 127:8954–8955.
51. Turro NJ (2000) From boiling stones to smart crystals: Supramolecular and magnetic isotope control of radical-radical reactions in zeolites. *Acc Chem Res* 33:637–646.